NJC

New Journal of Chemistry

A journal for new directions in chemistry

Accepted Manuscript

This article can be cited before page numbers have been issued, to do this please use: A. Kumar and P. Dhiman, *New J. Chem.*, 2019, DOI: 10.1039/C9NJ02949D.

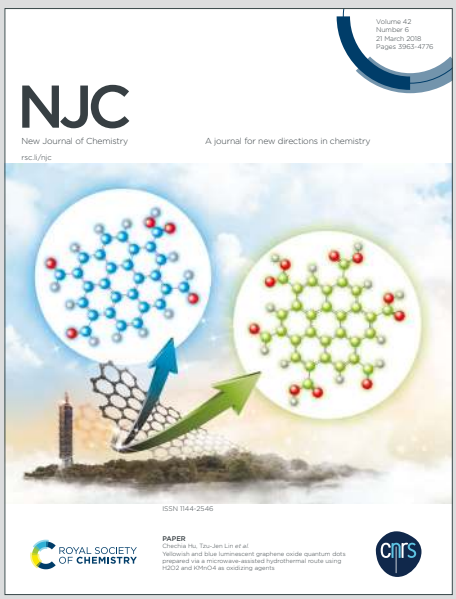

This is an Accepted Manuscript, which has been through the Royal Society of Chemistry peer review process and has been accepted for publication.

Accepted Manuscripts are published online shortly after acceptance, before technical editing, formatting and proof reading. Using this free service, authors can make their results available to the community, in citable form, before we publish the edited article. We will replace this Accepted Manuscript with the edited and formatted Advance Article as soon as it is available.

You can find more information about Accepted Manuscripts in the Information for Authors.

Please note that technical editing may introduce minor changes to the text and/or graphics, which may alter content. The journal's standard Terms & Conditions and the Ethical guidelines still apply. In no event shall the Royal Society of Chemistry be held responsible for any errors or omissions in this Accepted Manuscript or any consequences arising from the use of any information it contains.

View Article Online
DOI: 10.1039/C9NJ02949D

ARTICLE

Environmentally benign pH-responsive cytidine-5'-monophosphate molecule-mediated akaganeite (5'-CMP-β-FeOOH) soft supramolecular hydrogels induced by the puckering of ribose sugar with efficient loading/release capabilities

pHReceived 00th January 20xx,
Accepted 00th January 20xx

DOI: 10.1039/x0xx00000x

Anil Kumar* and Priyanka

The present manuscript reports the novel synthesis of 5'-CMP molecule-mediated pH-responsive porous supramolecular hydrogels consisting of β-FeOOH/5'-CMP core–shell type nanohybrids as a building block. As synthesized hydrogels has been fully characterized in terms of the size of the core, shape/morphology along with its optical, magnetic and rheological features. Interestingly, the gelation in the self-assembly is induced by the puckering of ribose sugar in 5'-CMP molecule enhancing the intermolecular non-covalent interactions between 5'-CMP of different nanohybrids as well as β-FeOOH in relatively a narrow pH (5.5-7; 7- 8.5) and temperature (35-40 °C) range. These changes have been analyzed by IR, Raman and CD spectroscopy. The viscoelastic nature of the optimized sample is revealed by fairly high values of viscosity (5.56×10^3 cP); G' (4×10^4 Pa), G'' (2.3×10^2 Pa) and a yield strain (8.1 %) with a linear viscoelastic region upto about 4%. A decrease in viscosity with shear rate demonstrates its gel like behavior matching to the soft supramolecular hydrogels. The mechanism of gel formation has been thoroughly analyzed. The pH, temperature as well as mechanical forces induced spontaneous transition(s) of sol into hydrogels and its complete reversal into sol suggesting it to be a smart material. Thus, the soft hydrogels consisting of the greener components like pyrimidine nucleotide (5'-CMP) and β-FeOOH phase, synthesized under physiological conditions of pH (7) and temperature (37 °C) with fairly high surface area, exhibiting self-healing, injectability, relatively higher %swelling (530), and efficient loading (217 mg/g) and release of adsorbed methylene blue (>98%; model drug) over a period of more than 3 days in aqueous PBS buffer, suggest it to be sustainable with significant biological and environmental potential.

Introduction

In recent year hydrogels are drawing increasing attention because of their porous nature and several interesting functional properties such as viscoelasticity, swelling, adsorption/loading and release capabilities.1-3 These characteristic features make them suitable to utilize for waste treatment [4-6] and different biomedical applications.[7-10] Hydrogels may be classified mainly as: (i). Classical - made from natural polymers/ biopolymers such as collagen, gelatine, silk fibroin, chitosan, DNA,[11] alginates, agarose, carbohydrates[12] and peptides,[13-15] (ii) Synthetic - employing polymers such as polyethylene glycol,[16] polyvinyl alchol,[17] polyacrylic acid and polyacrylamide.[6,18,19]

Other class of hydrogels, gaining more popularity, are referred to as molecular gels. Molecular based hydrogels are usually constructed synthetically from relatively smaller organic/biomolecules such as amino acids, sugar based components, and nucleotides.[20-29] These molecule(s) interact with each other through supramolecular interactions such as hydrogen bonding, van der Waals, pi-pi, cation-pi, electrostatic and hydrophobic.[30] Such soft molecular hydrogels are similar to natural self-assembled fibrillar nanosystems[31] and are well defined in terms of their components in contrast to the polymeric gel consisting of covalent bonds. Besides, soft molecular gels because of their enhanced flexibility, tunability, reversibility, biodegradability, adaptability and self-healing properties are finding increasing applications for wound healing, tissue engineering, cell culture and localized drug delivery[14] contrary to the polymeric gels, which often being brittle lack self-healing and reversibility.[32] Several such polymer based biocompatible supramolecular hydrogels have been

Department of Chemistry, Indian Institute of Technology Roorkee, Roorkee – 247667, India. E-mail: anilkfcy@iitr.ac.in; akmshfcy@gmail.com; Fax: +91 1332 273560; Tel: +91 1332 285799.

† Electronic supplementary information (ESI) available: Scheme1: Image of hydrogel formation steps. Figures: TGA (Fig. S1), UV-Vis spectra (Fig. S2), XRD of colloidal samples at pH 4.3 (Fig. S3), Zeta potential curve (Fig. S4), AFM Pore depth of SPC3H (Fig. S5), TEM image of freeze dried SPC3H (Fig. S6), FESEM image (Fig. S7), M-H and FC-ZFC plots (Fig. S8), Raman spectra of bare β- FeOOH and 5'-CMP (Fig. S9), IR spectrum of SPC3 at pH 4.3 (Fig. S10), XPS spectra of P and Cl elements (Fig. S11), BET curve (Fig. S12), Release curve of MB at pH 5.5 (Fig.S13), Sensing of alcohol image (Fig. S14), Adsorption and release curves of MB on FD gel (Fig. S15), Cell viability graph (Fig. S16), Rheological measurements of hydrogels at pH 5.8 (Fig. S17). Tables: Magnetic data(Table S1), Raman data (Table S2), IR data (Table S3), XPS data (Table S4), Rheological data at pH 7 (Table S5), BET data (Table S6), Rheological data at pH 5.8 (Table S7). See DOI: 10.1039/x0xx00000x.

‡The manuscript was written through equal contributions of both authors. Both authors have given approval to the final version of the manuscript.

View Article Online DOI: 10.1039/C9NJ02949D

reported to show fairly limited drug loading efficiency besides exhibiting cytotoxicity.[32-34]

Colloidal chemistry involving nanomaterials provides an interesting tool to synthesize hydrogels by controlling the process(s) of nucleation and growth employing a variety of templates.[35,36] The use of biomolecule capped colloidal nanohybrids to fabricate soft hydrogels furnishes a novel approach, which not only stabilizes and control the size of the core nanoparticles but shall also impart them the biocompatibility. Besides, the surface functional groups of the template will also allow to design new nanostructure(s)/superstructure(s) involving the core nanoparticles/nanoclusters in a bottom-up approach. The self-assembly of such nanohybrids might involve some extensive intermolecular interactions among functional groups of the template as well as the inorganic core. The resulting increased networking among nanohybrids could be exploited to form the hydrogels.

Natural components of nucleic acid such as nucleoside and nucleotides being biocompatible, exhibiting flexibility, programmability, and molecular recognition ability have tremendous potential for developing molecular gels for biomedical applications.[24-26] We have come across only a few reports on bare nucleotides based hydrogels involving guanosine monophosphate (GMP) molecule and adenosine monophosphate (AMP) molecule(s). These produced hydrogels in the presence of Ag^{+} and Zn^{2+} ions, respectively,[22-24,36] by making use of their fairly high concentration(s) (50/40 mM).[37,38] The pyrimidine based nucleotides (cytidine 5-monophosphate (5'-CMP) & uridine 5'-monophosphate(5'-UMP)) are, however, not known to produce hydrogels like nanostructures, possibly because of the poor interaction between the respective nucleobases as well as with the metal center.[24,29] For example, AMP and GMP, involved interactions through their different functional groups on pyrimidine and imidazole moieties, but on the contrary CMP could undergo interaction with metal center through N3 only. It is, therefore, challenging to produce hydrogels involving these nucleotides in aqueous medium.

Cytidine-5'-monophosphate (5'-CMP) is an important FDA approved component/building block[39] of nucleic acid (DNA/RNA) consisting of pyrimidine moiety attached to ribose sugar and phosphate group (Fig. 1). Pyrimidine based nucleotides are known to play a crucial role in metabolic functioning and 5'-CMP in particular has been reported to participate in the regeneration of the muscles and nerve fibers.[40] It also contributes to the child growth by being as one of the important constituents of the breast milk in human.[41,42]

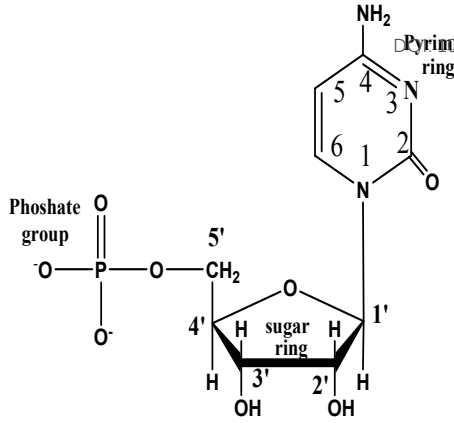

Fig. 1 Structure of cytidine 5'-monophosphate.

Iron oxide(s) based nanomaterials (in its various polymorphs) have been among the most widely investigated materials used for a variety of catalytic and biomedical application(s)[43-47] because of their magnetic and environmentally friendly nature. In particular, the akaganeite (β-FeOOH) with tunnel like structure with low toxicity/cytotoxicity (in vivo/ vitro),[48,49] biodegradability[48] and environmentally friendly nature[50] has been employed for several environmental[51-53] anion exchange,[54] catalytic,[55] sensing[56] and biomedical applications.[40,48,49]

In this manuscript we present hitherto unreported synthesis of 5'-CMP molecule-mediated β-FeOOH supramolecular hydrogels at physiological pH and temperature employing the colloidal approach. This system as a whole consists of the biocompatible components (5'-CMP and β-FeOOH) involving relatively lower concentration of template in a difference to polymeric gel(s). The β-FeOOH nanoparticles (NPs) nucleated in the early stages get coated with the biotemplate through non-covalent interactions to yield hydrogels in self-assembly involving the puckering of ribose sugar. As synthesized hydrogels has been characterized for the presence of inorganic component(s), their size, morphology, surface area along with their swelling, magnetic and viscoelastic behavior. It exhibited pH-, temperature- and mechanical force-responsive reversible transition from sol to gel and vice versa. The mechanism of these processes has been discussed. The loading/adsorption and release of certain dyes such as methylene blue (model drug - used for treating methemoglobinemia)[57,58] and Nile blue A (a potential photosensitizer employed for photodynamic therapy of malignant tumors, bioimaging and sensing),[59-61] have been performed in soft hydrogels at physiological pH 7. The as synthesized superparamagnetic hydrogels with fairly high values of viscosity, mechanical features (G', G'', and yield strain) as well as efficient loading (217 mg/g)/release capabilities qualify it to be an interesting soft material for biomedical applications. To the best of our knowledge this is the first report on hydrogels formation employing any pyrimidine based nucleotide(s). Such supramolecular hydrogels consisting of natural low molecular weight biomolecule(s) have immense potential for biomedical usage such as drug delivery, wound

View Article Online
DOI: 10.1039/C9NJ02049D

healing and tissue engineering because of their biocompatibility and stimuli responsive behavior[25] unlike to polymeric gel.

2 EXPERIMENTAL

2.1 Chemicals

The following analytical grade chemicals of different make: Merck - $FeCl_3$ anhydrous, KBr; Alfa Aesar – cytidine 5'-monophosphate disodium salt (5'- CMP); Himedia - $HClO_4$, phosphate buffered saline; BDH – NaOH; Thomas baker-methylene blue (MB); sigma- nile blue (NB). All these chemicals were used without further purification. The carbon coated copper grid and dialysis tubing (seamless cellulose tubing/dialysis tubing closures) were purchased from M/s Icon and Sigma, respectively. Millipore water having 18.2 MΩ conductivity at 25 ^{o}C has been used for the preparation of all the solutions.

2.2 Equipment

The absorption and fluorescence spectra of the samples were recorded on a Perkin Elmer (Model Lambda 950) UV-Vis-NIR spectrophotometer by using quartz cuvette of 2 mm path length and on a Shimadzu spectrofluorophotometer (Model (RF-5301pc). X-ray diffraction patterns of the powder samples were measured on a Rikagu X-ray diffractometer by using Co Kα line (1.78897Å) of the X-ray source at the scan rate 0.02 step/min. The Raman spectrum of the samples was recorded on an inVia Renishaw spectrometer (serial no.021R88 and H33197) equipped with a confocal microscope using Ar ion 514 nm laser source at 1% laser power and exposure for 60 s. The charge on the sample surface was recorded on a Malvern Instrument having 632 nm He-Ne laser as a light source equipped with NOVA software. The surface area and adsorption isotherm were obtained on an Autosorb-iQ2 instrument (Quanta chrome Instruments, USA at 77.350 K and the sample(s) were degassed at 100 ^{o}C for 5h. The elemental analysis of the surface of sample(s) was performed by X-ray photoelectron spectroscopy (PHI Versa Probe III electron spectrometer) (XPS) using: source Al K_α 1486.708 keV, step width = 0.05 eV, energy resolution = 0.5 eV, pass energy = 55 eV at a base pressure of 10^{-7} mbar. The Ar ion gun was used to clean and neutralize the specimen surface prior to record the XPS characteristic. FTIR spectra of the powder samples were recorded on a Perkin Elmer (FTIR) spectrophotometer in the mid-IR range (1800–400 cm^{-1}) in KBr media having a resolution of 0.5 cm^{-1}. The 2D and 3D images of the samples were recorded by atomic force microscope (AFM) purchased from NTEGRE (NTMDT) in semi contact mode. Field emission electron microscopy (Carl Zeiss) equipped with an energy dispersive (EDAX) accessory was employed for analysing the surface morphology and composition of elements of as synthesized samples by applying 15 kV accelerating voltage. Transmission electron micrographs, selected area electron diffraction (SAED) of the samples were recorded on a FEI-TECNAI G220 S-TWIN at 200 kV equipped with a CCD camera. The magnetic behaviour of the samples was analysed on a superconducting quantum interference device (Quantum Design MPMS-XL/MPMS-3) instrument(s) at different temperatures. The rheological study of the hydrogels sample was performed on a MCR 102 rheometer from Anton Paar using a cone−plate geometry with a diameter of 40 mm and a 1° cone angle at 20°C. The circular dichroism (CD) spectra of sample(s) were carried out at room temperature on a Chirascan spectropolarimeter procured from Applied Photophysics, United Kingdom. All the reactions were carried out on a silicon oil bath fitted with a temperature controller (Medica instrument MFG., CO). The pH of solution(s) was measured by using a 510 pH meter supplied by Eutech instrument. Solvent (water) from the sample(s) was removed by using a rotary evaporator (IKA RV10) and, thereafter were fully dried in an oven at 70 ^{0}C. The centrifugation of the gel samples was carried out on a REMI microprocessor research centrifuge (Model PR -24) at 5000 rpm for 20 min. The loading/adsorption of dyes was carried out by using a water bath shaker (NSW, NSW-133, India) at room temperature at a low shaking speed. The gel samples were sonicated using an ultrasonicator (Metrax) at room temperature.

2.3 Methodology

The 5'-CMP molecule-mediated β-FeOOH nanoparticles were synthesized by adding varied [5'- CMP] (0.5 - 5 mM) to $FeCl_3$ (30 mM) in 100 ml deionized water (DIW). The reaction mixture was hydrolysed at 100 ^{o}C for 6 h using a silicon oil bath following previously developed protocol for other biotemplated hydrogels.[35] After the completion of reaction, the samples were cooled at room temperature and the excess of reactant(s) were removed by performing dialysis in DIW.

An interesting observation noted about this system was that an increase in the concentration of 5'-CMP beyond 0.5 mM only resulted in the formation of hydrogel. Moreover, the gelation time was found to decrease with an increasing 5'-CMP and is observed to be dependent on both the pH as well as the temperature. At low pH as synthesized particles remained as colloidal solution and could be transformed rapidly into the supramolecular hydrogels in a narrow pH (5.5 to 7 and 7 to 8.5) and temperature (35 - 40 ^{o}C) range. In the present study we have optimized the sample by maintaining the pH and temperature at 7.0 and 37 ^{o}C, respectively; *i.e.* under physiological conditions. As synthesized colloidal sample(s) containing different amount of 5'- CMP (mM) have been labelled as: SPB (0.0); SPC1 (0.5); SPC2 (1.5); SPC3 (2.5); SPC4 (3.5); SPC5 (5.0) and the hydrogel sample(s) are abbreviated as: SPC2H (1.5); SPC3H (2.5); SPC4H (3.5).

The entire synthesis process of the hydrogel formation is shown in scheme S1. The stability of the as synthesized samples (SPB, SPC3, SPC3H) were analysed by performing TGA (Fig S1). The loading and release of MB and NB dyes were performed by following their absorption and fluorescence, respectively. The amount of adsorbed and released MB and NB were measured by monitoring the absorption of MB at its λ_{max} (665 nm) and emission of NB at its $\lambda_{em,max}$ 667 nm using λ_{ex} 635 nm, respectively.

View Article Online DOI: 10.1039/C9NJ03040D

2.4 Preparation of samples for various characterization

For recording of the electronic and CD spectra, the as synthesized hydrogel samples were diluted by about 100 times using DIW. For IR, Raman, XRD, BET, XPS, TGA and magnetic measurements, the freeze dried (FD) solid sample was employed. For rheological study the centrifuged soft molecular hydrogel samples were used. For AFM and FESEM measurements the diluted samples were drop casted on a glass slide and dried overnight in dark at room temperature. For TEM analysis the diluted sample was applied on to a carbon coated copper grid and dried overnight at room temperature. Zeta potential measurements were carried out by using as synthesized colloidal solution without dilution. For magnetic measurements the weighed amount of sample was filled in a starch capsule to about 2/3rd of its space and the empty portion was packed with the cotton. For IR spectral measurements about 5 mg of the sample was mixed with KBr and prepared a pallet by using the palletizer.

2.5 Cytotoxicity analysis

The cytotoxicity of the as synthesized hydrogels was examined by performing the MTT assay employing the 293T human embryonic kidney cell. These cells were grown in 96 wells plate up to 4000 cells per well in 24 h. Different sample size ranging from 62.5 µg/µl to 500 µg/µl were added to the 96 well plates in triplicates for which an equal volume of DMSO has been used as a control in triplicates. The plates were then incubated in 5% CO_2 for 48 h. After that 20 µl of 5 mg/ml MTT solution was added to each of these wells and incubated for 2 h, then 100µl of DMSO was added to each of the wells to dissolve the crystal. The absorbance due to these samples were recorded colorimetrically.

3. Results

3.1 Optimization of 5'- CMP concentration for hydrogels formation

A change in the [5'- CMP] in colloidal solutions from 1.5 to 5 mM influences the time of gelation in a complex process. Initially, an increase in the [5'- CMP] up to 2.5 mM reduced the time of gelation from 10 days to 4 days. Thereafter, a further increase in 5'- CMP brought a partial gelation only. For all the samples gelation was associated with a change in pH from 4.3 to 5.8. Hence, 2.5 mM of 5'- CMP has been considered to be the optimum amount for the formation of hydrogels.

3.2 Effect of [5'- CMP] on the optical absorption of colloidal iron oxide based nanostructures

The absorption spectra of as synthesized fresh colloidal solutions of iron oxy hydroxide containing varied [5'- CMP] are shown in Fig. S2. These peaks differ to those of its individual components (nm): 5'- CMP (235 and 272) and β-FeOOH (288 and 345), respectively recorded under identical experimental conditions (Fig. S2). An increase in [5'- CMP] was noted to enhance the absorption coefficient above 400 nm associated with a reduction below 400 nm. In the same figure a comparison of the absorption spectrum of SPC3 with that of bare β-FeOOH reveals that the former display relatively higher absorption coefficient in the visible range up to 400 nm and, thereafter it depicted lower absorption in the shorter wavelength range.

Fig. 2 shows the absorption spectra of the SPC3 (pH 4.3) (curve a); SPC3H (curve b) along with that of 5'- CMP (curve c) at pH 7. The absorption spectrum of SPC3H has been recorded by bringing it in the liquid form upon vigorous shaking. The absorption spectra of SPC3 and SPC3H exhibited peaks (nm) at: 275; 354 and 490, which can be assigned to the ligand based transition; ligand field d-d transition of Fe3+ and Fe-Fe pair, respectively. A comparison of UV-Vis spectrum of SPC3 and SPC3H shows that the Fe-Fe pair coupling for both the samples shows very similar absorption behaviour except that the crystal field splitting absorption arising due to d-d transition becomes less pronounced for the later. Moreover, it depicted an isosbestic point at 513 nm and exhibiting relatively higher absorption coefficient beyond 518 nm along with a simultaneous decrease in the absorption coefficient at lower wavelengths (Fig. 2, Inset).

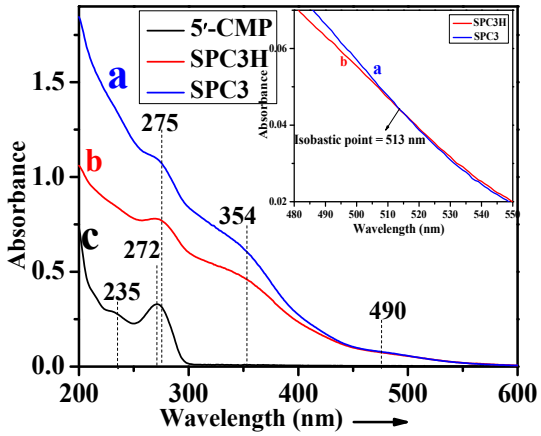

Fig. 2 UV-Vis spectra of SPC3 (a); SPC3H (b); 5'- CMP (c) and Inset: enlarge curve exhibiting the isosbestic point between curve a and b.

3.3 XRD

The XRD patterns of all the colloidal samples containing varied [5'- CMP] (0.5 – 5 mM) are shown in Fig. S3. The indexing of these diffraction patterns showed various peaks at 2θ values - 13.8, 19.2, 31.1, 41.1, 46.3, 54.9, 66.8 and 72.8 corresponding to (101), (200), (103), (112), (013), (114), (215) and (116) planes, respectively and fairly matches with the monoclinic structure of β-FeOOH (JCPDS file 80-1770). An examination of these patterns indicate the resolution of the peaks to become poorer beyond 2.5 mM of 5'- CMP.

The XRD patterns of both SPC3 and SPC3H (Fig. 3, curves a and b) matched with the JCPDS file (80-1770) and exhibited the higher intensity at 2θ value of 31.1° and 41.1° analogous with its (103) and (112) planes unlike to that of (101) plane reported for the respective bulk. A comparison of the diffraction patterns due to SPC3 and SPC3H reveals that the latter sample shows a significant reduction in the intensity of the peaks corresponding to different planes suggesting the more effective coating of 5'- CMP on β-FeOOH in the hydrogel sample.

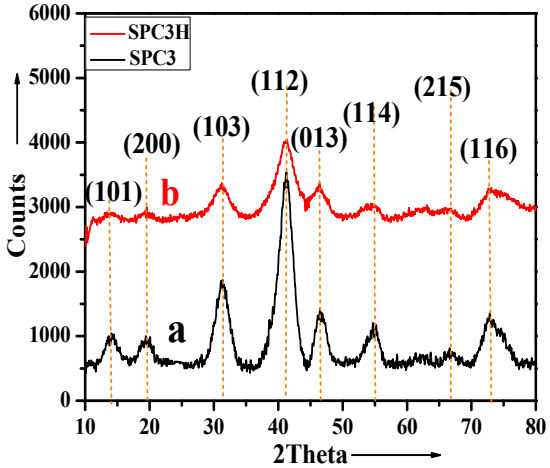

Fig. 3 XRD patterns of SPC3 at pH 4.3 (a); SPC3H at pH 7 (b).

3.4 Stability of colloidal solution - Effect of pH

The stability of colloidal solution of SPC3 was also examined by monitoring the zeta potential (ζ) of the colloidal solution as a function of pH (Fig. S4). A variation in pH from 2.7 to 11.0 brings a change in the value of zeta potential (ζ) (mV) from (+) 39 to (-) 32. At pH 7 the value of ζ was estimated to be about (-) 28 mV, which suggests SPC3 to be fairly stable at this pH. Interestingly, at this pH the gel formation is initiated within 5 min unlike to that at lower pH, which needed a period of about 4 days. The process of gelation is not energy intensive as it occurs at room temperature under physiological conditions. Since pH 7 is considered to be the most appropriate for the biological applications hence, all experiments have been performed at pH 7.

3.5 AFM analysis

Fig. 4 shows the representative AFM images of SPC3 and SPC3H. An analysis of these images reveals the formation of largely the chains of nanoparticles in SPC3 and porous structure for SPC3H at pH 7. The surface roughness of SPC3 was found to be about 8.2 nm with a roughness distribution ranging from 2 to 14 nm. Interestingly, for SPC3H, its 2D image exhibits the fibrous/porous nanostructures with a pore depth of 7 ± 1 nm (Fig. S5) possibly due to rearrangement of the nanoparticles in the hydrogel. Their average roughness (roughness distribution) was found to be 12 nm (6 to 20 nm).

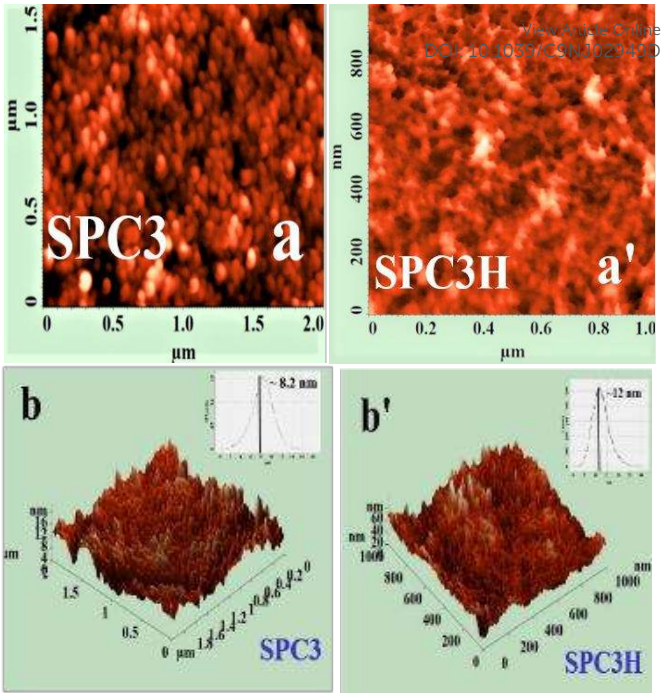

Fig. 4 AFM images of SPC3 and SPC3H: 2D image (a, a'); 3D image with roughness (inset) (b, b') respectively.

3.6 Transmission electron microscopy (TEM)

TEM micrographs of SPC3 and SPC3H are shown in Fig. 5. The TEM images due to SPC3 shows the formation of nanoparticles with an average size (nm) (size distribution) of 5 (3 - 7). These nanoparticles are joined together to form a chain like structure. SAED analysis of these particles shows the formation of diffused rings masked with spots. The indexing of this pattern corresponded to reflections from (101), (200), (103), (002), (202), (301) and (112) planes due to β-FeOOH matching with the JCPDS file (80-1770). HRTEM image of these particles (Fig. 5A'') shows the d- spacing 0.763 nm matching to the (101) plane of β-FeOOH. Whereas, in SPC3H (Fig. 5 B) these particles grow to yield relatively bigger clusters containing core-shell type nanostructures, which get folded to form the porous structure. From this micrograph the average size (size distribution) of the dark core nanoparticles was estimated at 15 ± 5 nm (10-20). SAED pattern due to SPC3H exhibited the relatively distinct ring pattern with much brighter spots to than that of the fresh sample (SPC3). The indexing of this pattern shows the presence of (101), (200), (400), (110), (112) and (103) planes matching with the β-FeOOH phase. This finding indicates that the crystallinity of these nanoparticles increase in the process of gelation. After gel formation the HRTEM image of SPC3H shows the d spacing 0.33 nm corresponding to (103) plane of β-FeOOH.

.

View Article Online
DOI: 10.1039/C9NJ02949D

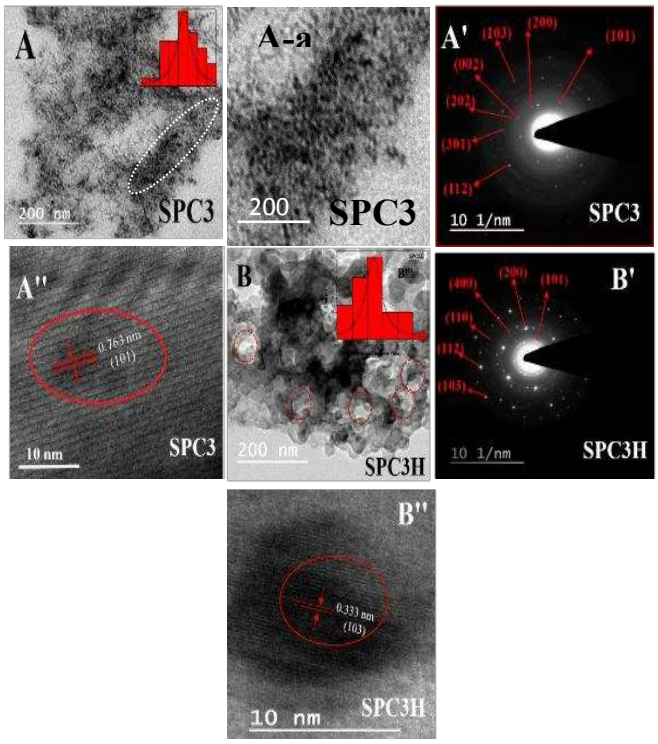

Fig. 5 TEM images of SPC3 and SPC3H (A, B) and enlarge image of a portion of A marked in red (A-b); SAED pattern (A', B'); HRTEM (A'', B''); Size distribution bar diagram (A''', B'''), respectively.

TEM and FESEM images of freeze-dried gel have also been recorded (Fig. S6 and S7) which clearly show its porous nature.

3.7 Magnetic study

The magnetic behaviour of SPC3H was examined by recording M-H curves at three different temperatures: 300, 100 and 5 K with a variation in magnetic field from 0 - 7 tesla (Fig. S8A, Table S1). A decrease in temperature resulted in an increase in magnetization. At 300 K (RT) the M-H curve at lower field showed almost a linear increase in magnetization with an increase in magnetic field (H) up to 3.5 T and starts taking a plateau value beyond this field. At 100 K the magnetization value initially shows linearity but starts attaining a plateau at much lower value of H (1.3 T). Both of these curves at 300 and 100 K exhibited reversible behaviour with a negligible coercivity and remanence. However, at 5 K M-H curve becomes irreversible with a remanence (M_r) and coercivity (H_c) values of 0.63 emu/g and 0.3 T, respectively (Fig. S8B). The magnetic behaviour due to SPC3H was further probed by recording FC-ZFC measurements in the temperature range of 5 to 300 K at two external magnetic fields of 100 O_e and 500 O_e (Fig. S8C; curve a and curve b). At lower external magnetic field (100 O_e) the FC and ZFC curves showed the splitting (T_s) at 165 K. Whereas, in ZFC curve the blocking temperature (T_B) and in FC curve the Neel temperature ($T_{N)}$ were observed at about 53 and 45 K (Fig. S8C, curve a), respectively. Notably, the FC curve was found to cross the ZFC curve at relatively lower value of magnetization. However, at 500 O_e it exhibited a maximum in the ZFC curve at about 41.5 K corresponding to the blocking temperature T_B without the FC curve crossing the ZFC curve. Above this temperature these nanostructures depicted superparamagnetic behaviour.

The observation of relatively smaller magnetization (2.4 emu/g) at 300 K in the as synthesized SPC3H and the reversibility of the M-H curve under the applied magnetic field of 7 T suggest that the magnetization might have arisen possibly due to both paramagnetic as well as superparamagnetic components under these conditions.

For β-FeOOH nanoparticles the uncompensated spin and magnetic disorder have been assigned earlier to be responsible for paramagnetic behaviour in the high temperature range, and the uncompensated spin in the superparamagnetic regime at relatively lower temperature.[62] The magnetic behaviour has also been verified by drawing a plot M vs H/T in which these curves are observed to be roughly coincident up to the applied field of about 1 T, suggesting the contribution of superparamagnetic behaviour in these nanostructures (Fig. S8D). In the temperature range below 60 K it starts showing a departure from superparamagnetic behaviour as was indicated by the irreversibility in the hysteresis loop, which suggests that a large fraction of uncompensated spin is frozen under these conditions (Fig. S8a and S8b). In these smaller size particles, the ferromagnetic nature at lower temperature might have been contributed due to the surface and shape anisotropy.

The β-FeOOH in SPC3H exhibited superparamagnetic behaviour, which is different to its antiferromagnetic nature in the bulk (Fig. S8A). This change in behaviour is understood to arise because of the binding of 5'-CMP with β-FeOOH surface in SPC3H, which removes the uncompensated spin. This phenomenon becomes more prominent at relatively higher magnetic fields as is evident both by M-H plots which started taking plateau value at 3.5 T (Fig. S8A). It is further validated by the M-T plots in which FC curves recorded at 100 O_e and 500 O_e, where these curves reveal that at 100 O_e, the magnetization value near the T_B (recorded from ZFC curve) was smaller to that of at 500 O_e. It is understood due to the presence of uncompensated spins left in β-FeOOH nanohybrids at lower external magnetic field. A shift in the value of T_B from 53 to 41.5 K at higher external magnetic field of 500 O_e (Fig. S8C) and a linearity of M vs H/T (Fig. S8D) further supports its superparamagnetic behaviour. Such observations have also been attributed earlier to the superparamagnetic behavior.[35]

3.8 Raman spectroscopy

The Raman spectra of SPC3 and SPC3H have been recorded to analyse the phase observed in XRD (Fig. 6a and 6b). SPC3 and SPC3H displayed peaks (cm^{-1}) at: 316 (broad (br)), 388(br), 535(br), 731, 796, 987(br), 1062(br) and 1309 (br); 322(br), 398, 535(br), 731, 792, 838(br), 948(br), 978, 994, 1007(br), 1071, 1093(br), 1113, 1149(br), 1182, 1263(br) and 1291(br). In Fig. 6, the peaks (cm^{-1}) marked in black matches to that with the β-FeOOH phase and rest other peaks marked in red are

View Article Online
DOI: 10.1039/C9NJ02949D

contributed by 5'-CMP, as was ascertained by recording the Raman spectra of the respective bare sample(s) in a control experiment (Fig. S9a and S9b, Table S2). These Raman bands clearly ruled out the presence of peaks (cm^{-1}) due to other phases like: α-FeOOH (162, 297, 384, 477, 545 and 655), γ-FeOOH (140, 214, 249, 284, 345, 374, 524 and 647) and Fe_3O_4 (295, 521 and 662).[63]

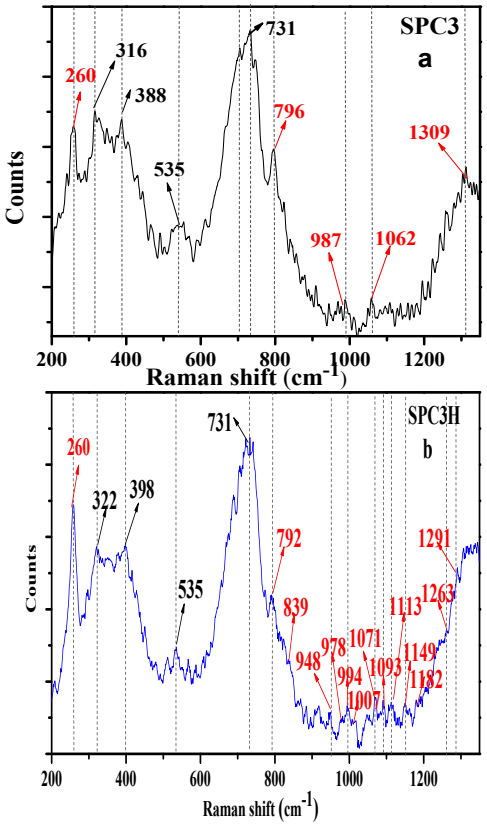

Fig. 6 Raman spectra for (a) SPC3; (b) SPC3H.

Apart from the above the Raman spectrum of SPC3H shows the development of two new bands (cm^{-1}) at 978 and 994 in contrast to the pure 5'-CMP (Fig. S9b), which shows a mild Raman band at 986 cm^{-1}. Some weak bands were also observed at 1007 to 1071 cm^{-1}, which are very likely to be contributed due to rotationally resolved Raman bands.

3.9 IR spectroscopy

An analysis of interaction of 5'-CMP with β-FeOOH phase in SPC3H has been carried out by recording its FTIR spectrum in the wavenumber range of 400 to 1800 cm-1 (Fig. 7; curve a) along with the spectra of pure 5'-CMP (Fig. 7; curve b) and bare β-FeOOH (Fig. 7; curve c) under identical conditions of pH and their spectroscopic data have been compiled in Table S3.

The FTIR spectrum of SPC3H exhibited various bands (cm^{-1}) at: 473 (br), 651(br), 707(br), 790, 852(br), 984, 1066(br), 1113(br), 1216, 1286, 1345, 1491 (br), 1535, 1632(br) and 1653(br) (Fig. 7a).

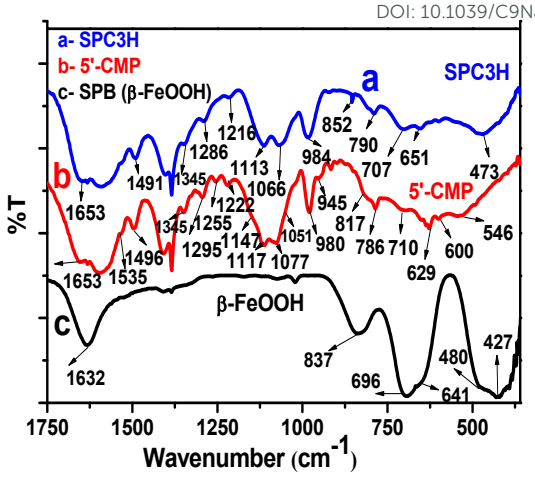

Fig. 7 FTIR spectra for (a) SPC3H; (b) 5'-CMP; (c) SPB.

In control experiments, the spectrum due to 5'-CMP shows several peaks (cm^{-1}) due to its different functional groups, matching largely with the literature data (Fig. S10, Table S3).[64-67] IR peaks due to bare β-FeOOH observed at (cm^{-1}): 427(br), 480, 641(br), 696(br), 837, and 1632(br) also matched with the previous reports.[68]

A careful comparison of the IR spectrum of SPC3H with bare 5'-CMP and β-FeOOH phase shows it to contain absorption at fairly different frequencies as compared to its individual components (Table S3, column VII). Some of the bands (cm^{-1}) observed at: 473 (br), 651(br), and 707(br), which are as such not present in either of the IR spectra due to pure 5'-CMP and/or β-FeOOH, are possibly contributed due to the interaction of β-FeOOH with 5'-CMP in the self-assembly. The interaction of β-FeOOH with 5'-CMP in SPC3H through its Fe^{3+} center is indicated by FTIR spectroscopy by the disappearance of peaks due to: Fe — OH ------- Cl (837cm^{-1}), P-O str. (817 cm^{-1}), $-NH_2$ (1147 cm^{-1}) and ribose sugar (873, 941 cm^{-1}), respectively along with the simultaneous development of a new peak at 852 cm^{-1} (δ(C2'-Cl'-O4')) (Fig. 7; Table S3). Besides these, unlike to FTIR spectrum of pure 5'-CMP (Fig. 7b; Table S3), which exhibited a broad band in the wavenumber range of 1040 - 1150 cm^{-1}, it shows two peaks (cm^{-1}) at 1113 (m, br; νC4'O-νC4'C3'-δ C3'O3') and 1066 (m, br), and the peak at 980 cm^{-1}(s) becomes broader and moved to higher energy at 984 cm^{-1}. All these changes have been assigned to the binding of Fe^{3+} of β-FeOOH mainly through **N** containing functional groups, ribose sugar as well as PO_3^{2-} of 5'-CMP molecule(s).

3.10 X-ray photoelectron spectroscopy

The surface analysis of as synthesized SPC3H and SPC3 nano-structures were performed by using XPS. The survey scans of both of these samples were recorded in the binding energy range 0 to 800 eV exhibiting the presence of elements: Fe ($2p_{3/2}$, $2p_{1/2}$), O(1s), N(1s), C(1s), P(2p), and Cl(2p) (Fig. 8, Panels A and A').

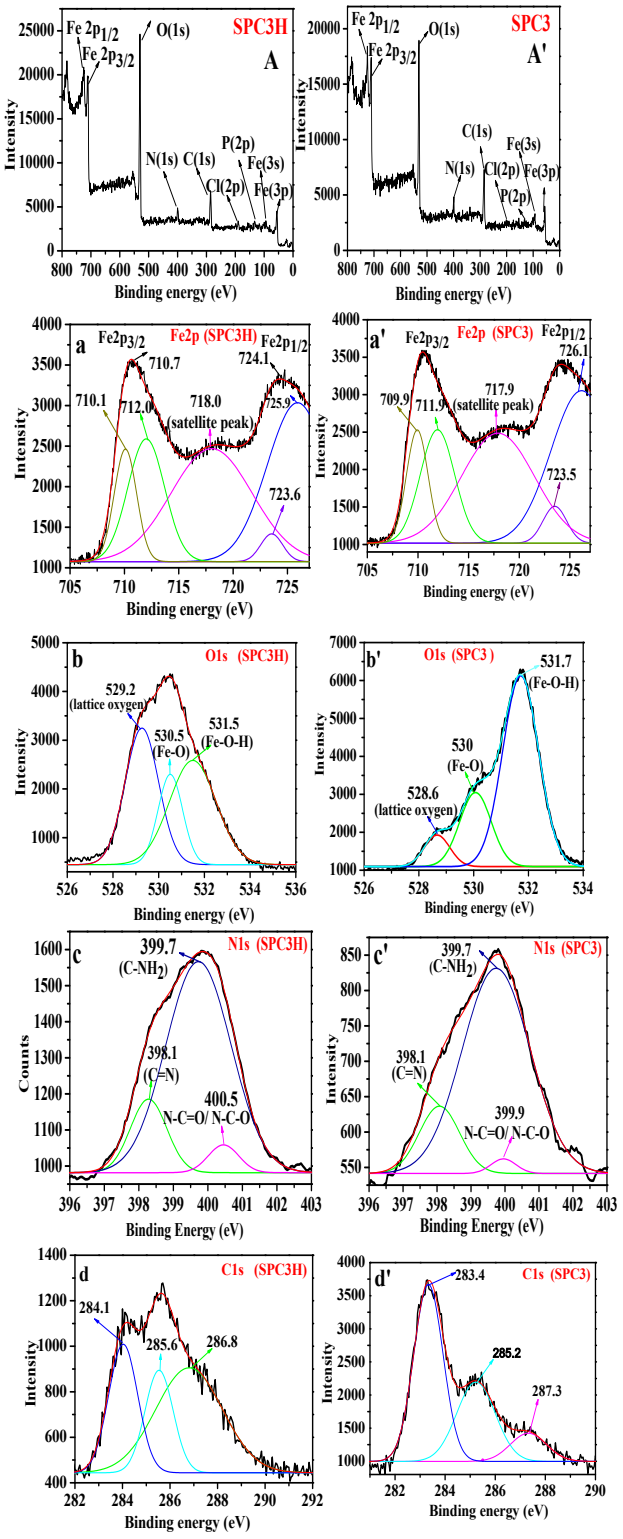

Fig. 8. XPS spectra: survey scan of SPC3H and SPC3 (A, A'); narrow range scan of Fe2p (a, a'), O1s (b, b'), N1s (c, c'), C1s (d, d'), respectively.

The spectra of elements of SPC3H and SPC3 (Fe, O, N, C) have been further probed in the narrow energy range and have been presented in different panels from **a** - **d** and **a'** - **d'**, respectively (Fig. 8). An analysis of panel **a** exhibits peaks at 710.7 and 724.1 eV along with a satellite peak at 718.0 eV with a spin-orbital coupling of 13.6 eV matching with Fe ($2p_{3/2}$) and Fe ($2p_{1/2}$) peaks, respectively and each of these energy levels shows a splitting into two components each (710.1, 723.6; 712.0, 725.9). Each pair depicted almost similar spin-orbital coupling separation of 13.7 ± 0.2 eV. The analysis of other elements has been shown in Fig. S11.

A careful examination of the surface elemental analysis data of SPC3H and SPC3 in XPS (Table S4) shows that the intensity of peaks due to different elements in SPC3 were higher except to that for **N,** as compared to that of SPC3H. It not only indicated an increased fraction of N species in SPC3H to be now prominently present on the surface but also the peaks due to C=N and N-C=O/ N-C-O get shifted slightly towards higher binding energies as compared to SPC3 (Fig. 8). It clearly suggests a possibility of stronger interaction of β-FeOOH through increased nitrogen containing functional groups present on its surface besides other groups. This observation is in line to the IR spectral data discussed above.

3.11 Circular dichroism spectroscopy

The chirality of SPC3H was analyzed by recording its CD spectra at pH 7 (Fig. 9, curve a) along with that of bare 5'-CMP (Fig. 9, curve b) under identical conditions. The CD spectrum of SPC3H exhibited several peaks (nm) at: 195, 210, 256, 269, 279, 303, 318 with positive ellipticity and 202, and 239 with negative ellipticity. Whereas, the CD spectrum of bare 5'-CMP showed three peaks centered at (nm): 272(br); 219(br) and 197(br), with both positive and negative ellipticity, respectively matching fairly well with the previously reported CD spectrum of 5'-CMP.[69,70]

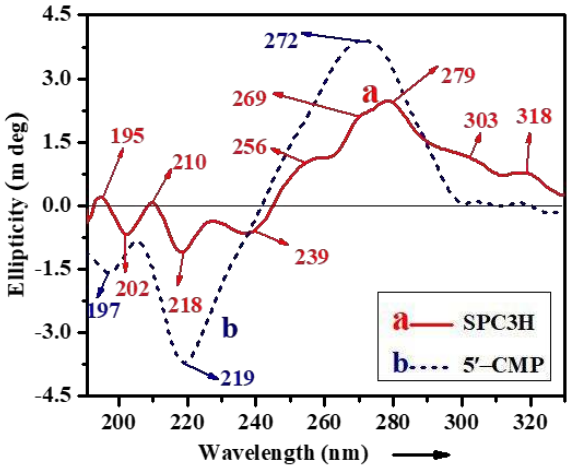

Fig. 9 CD spectra of (a) SPC3H; (b) 5'-CMP at pH 7.

View Article Online
DOI: 10.1039/C9NJ02949D

A comparison of CD spectrum due to SPC3H with that of 5'-CMP clearly shows the development of several new peaks with positive and negative ellipticity apart from a change in their magnitude(s) indicating the occurrence of new transitions in hydrogel sample.

Further the appearance of broad peaks (nm) with positive ellipticity (318, 303, 279, 269, 210 and 256), a reduction in values of ellipticity (218 and 202), and the development of a peak at 239 nm with negative ellipticity apparently suggest the new transition(s) to arise due to the twisting of sugar due to increasing non-covalent interactions in hydrogel.[71]A change in configuration of 5'-CMP is also evidenced by increased Π- Π* transition resulting in the red shift of the 272 nm peak to 279 nm upon formation of SPC3H. These changes suggest the presence of various associated structure(s) in hydrogels involving intermolecular interactions between 5'-CMP molecule(s) of different building blocks as well as with the β-FeOOH through its Fe center (Fig. 9).

Other changes arising due to the interaction of 5'-CMP and β-FeOOH are presented below (under discussion) along with the Raman, IR and CD spectroscopic data.

3.12 Rheological properties

The stability of the hydrogels was further examined by monitoring the viscosity as a function of: (i) time at a fixed shear rate (100 s^{-1}) (ii). Shear rate varied from 1-100 s^{-1}. The initial value of viscosity follows the order: SPC4H < SPC2H < SPC3H (Fig. 11A) and for all the samples it was found to decrease with time as well as upon increasing the shear rate (Fig. 10A') clearly indicating the formation of hydrogels in all these samples.

In order to optimize the viscosity and mechanical behaviour of hydrogels, rheological measurements were performed as a function of [5'-CMP] (1.5 to 3.5 mM) at pH 7.0 (Fig. 10; Table S5).

As regards to the dynamic mechanical behaviour of all the samples, the storage modulus (G') was always higher than that of the loss modulus (G'') (Table S5) and followed the order: SPC4H < SPC2H < SPC3H (Fig. 10B). A slightly higher values of G' and the yield strain for SPC3H to those of SPC2H and SPC4H suggests that the extent of cross linking to be more extensive in SPC3H. It is also indicated by the higher value of linear viscoelastic range (LVR) in case of SPC3H (4%) as compared to SPC2H (2.5 %) and SPC4H (1.5%) (Table S5).

G' and G'' as a function of shear stress at fixed frequency 1 Hz and a variation in the G' with angular frequency range of 0.1 to 100 rad/s at a fixed strain (0.5%) are shown in Fig. 10C and Fig. 10D, respectively.

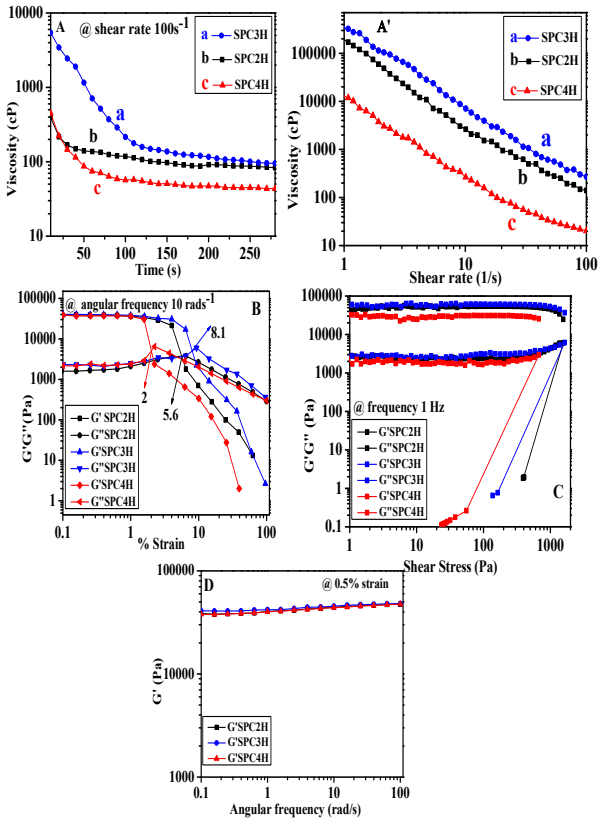

Fig.10. Rheology measurements for various hydrogels samples as indicated in each panel: (A) viscosity at a fixed shear rate 100 s-1; (A') viscosity profile for the shear rate sweep; viscoelastic behavior of gel - (B) amplitude sweep at fixed angular frequency 10 rad s-1; (C) G'G'' vs shear stress at frequency 1 Hz; (D) frequency sweep at a fixed strain 0.5%.

Among all the samples, SPC3H exhibiting the highest shear stress stability as well as the G' value in the entire angular frequency range (Table S5) demonstrate the best rheological features. These observations clearly indicate that the 3D structure of SPC3H hydrogels is fairly stable under the used experimental conditions.

3.13 Self –healing and injectable properties

In order to examine the self-healing feature of SPC3H, an experiment was designed using the centrifuged hydrogels sample. One portion of it was cut (Fig. 11 A-a) and then brought in close contact for healing, which took < 3 min for self-healing (Fig. 11 A-a'). Its injectable feature was analysed by employing the mechanical force on the hydrogels to produce the colloidal solution. This solution could be used for writing purpose on a glass slide, clearly demonstrating its injectable property (Fig. 11B). Such features have significant potential for their biomedical applications.

View Article Online
DOI: 10.1039/C9NJ02949D

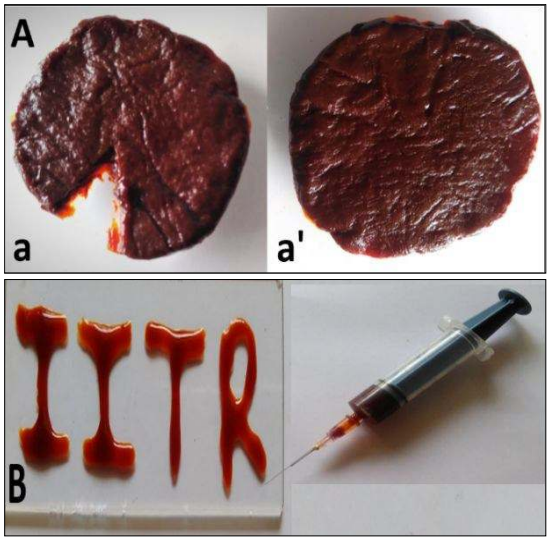

Fig. 11 Properties of soft hydrogel (A) self-healing; (B) injectability.

3.14 Swelling of hydrogels

The porosity in the hydrogels was measured gravimetrically by following the uptake of water. The percentage swelling of soft (dehydrated wet) as well as FD hydrogels is recorded as a function with time at room temperature for 13 h in the aqueous PBS buffer having pH 7 (Fig.12).

The percentage swelling has been calculated by using the following equation.

$$\%Swelling = \frac{W_s - W_D}{W_D} \times 100$$

W_s = weight of swollen gel, W_D = weight of dehydrated wet/dry gel

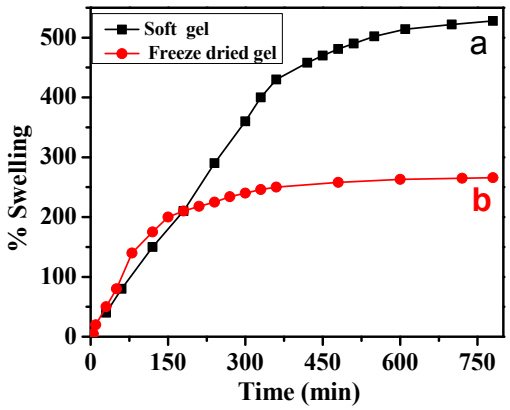

Fig. 12 %Swelling of (a) soft; (b) FD hydrogels in PBS at pH 7 after 13 h.

An examination of this plot showed almost a linear rapid increase in the % swelling initially and, thereafter it becomes fairly slow and take much longer time to attain the plateau value. From this curve the % swelling has been evaluated to be 530 and 266 for the soft and FD hydrogels, respectively. It suggests that the soft gel contains about twice the more porosity to that of FD gel.

The surface area of the FD gel was also determined by performing BET measurements (Fig. S12a, Table S6). Its adsorption isotherm curve depicted Type IV behaviour. Interestingly, DFT analysis of pore size distribution exhibited SPC3H surface to contain both micro- (1.2 nm) as well as mesoporous (4.7 nm) pores (Fig. S12b). The surface area and pore volume obtained from these measurements are 269 m^2/g and 0.31 cc/g, respectively. Obviously, the surface area of soft hydrogel would be much higher to that of the FD gel as noted by its much higher percentage swelling.

3.15 Loading and release capabilities of certain biologically important drug/dye

The porous nature of soft hydrogels (SPC3H) was further explored by the loading of MB (30 to 2000 µM) on its surface at 37 ˚C. The amount of adsorbed MB on the hydrogel surface as a function of its concentration shows it to follow almost linear relationship up to about 500 µM (94 mg/g) and, thereafter at higher concentrations the secondary adsorption starts showing an exponential increase in its adsorption, which correlates to about 217 mg/g of MB at 2000 µM (Fig. 13A). From these data the loaded amount of MB corresponds to 0.16 and 0.34 mg/ml respectively.

The loaded amount of drug/dye molecule in mg/g has been calculated by using the following formula:

$$\text{Loading amount } q_e(\text{mg/g}) = \frac{(C_0 - C_t)}{\text{m}} \times \text{V}$$

Where C_0 (mg/L) = initial dye concentration, C_t (mg/L) = dye concentration at time t, V = volume of the dye solution (L), m= weight of the adsorbent (g).

A significantly higher loading of MB on the soft gel is understood to arise due to the electrostatic interactions between positively charged dye and negatively charged hydrogels (SPC3H) at pH 7 (Fig. 13). This interaction was further probed by recording the release profile for relatively lower amount of the loaded drug (78 mg/g) into the medium of varied pH (5.5- 8.5) (Fig. 13B). It may be pointed out that in the higher concentration range MB undergoes dimerization as was ascertained by recording its electronic spectra (not shown).

An examination of the curves in Fig. 13B shows that the release was relatively much faster in the basic and slower in the acidic pH range. The release profile at different pHs (%release) followed the order: 5.5 (59) < 7 (>98) < 8.5 (>99). In all the cases the release was initially faster and prolonged over more than 3 days. Moreover, the release at all the pH values reached almost to completion. As expected, the dye encapsulation was the highest at pH 5.5 and lowest at pH 8.5, which is understood by the manipulation of charge on the hydrogel surface and loaded drug resulting in changed supramolecular interaction(s) between them in differing pH range. At pH 5.5 the release was much slower and took more than 30 days (Fig. S13). Notably, a comparison of the rate of release at pH 7 for different amount of loaded model drug shows the rate becomes slower for the lower amount of dye, which is an interesting observation in context of its usage for drug delivery. Similar observations about

View Article Online
DOI: 10.1039/C9NJ02949D

loading and release were made with positively charged dye NB at pH 7 (Fig. 13C and 13D). Digital images depicting incorporation of MB (A) and NB (B) molecules into colloidal SPC3 followed by their gelation at pH 7 and release are shown in Fig. 14.

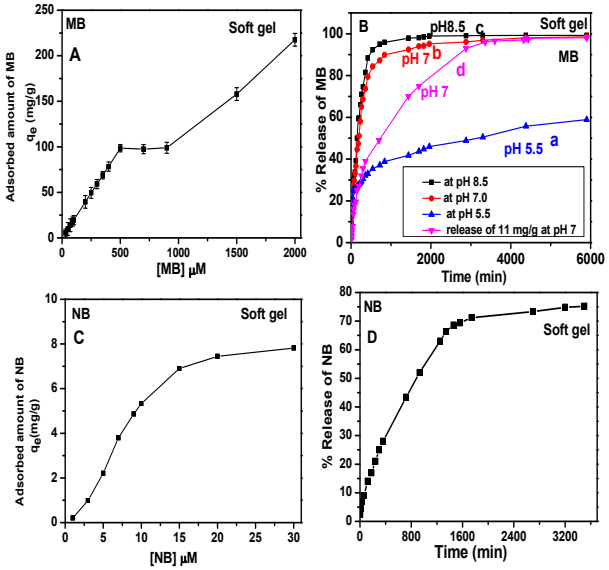

Fig. 13. (A) Adsorption isotherm of MB on soft gel; (B) Release profile of MB (78 mg/g): at pH 5.5 (curve a), pH 7.0 (curve b), pH 8.5 (curve c); release profile of MB (11 mg/g) at pH 7.0 (curve d). (C) Adsorption isotherm of NB on soft gel; (D) release profile of MB (7 mg/g) at pH 7.

After the complete release of dye, the matrix (SPC3H) could be reused for the adsorption/release of dyes. The adsorption of MB and NB has also been explored previously .[72,73] However, there is no data available for its release in most of the reports (vide infra, Table 1B). The NB loaded gel matrix also exhibited the sensing capabilities for alcohol, which showed a change in color from blue (in its absence) to pink in its presence (Fig. S14). The quantitative analysis for the detection of alcohol will be carried out in future work.

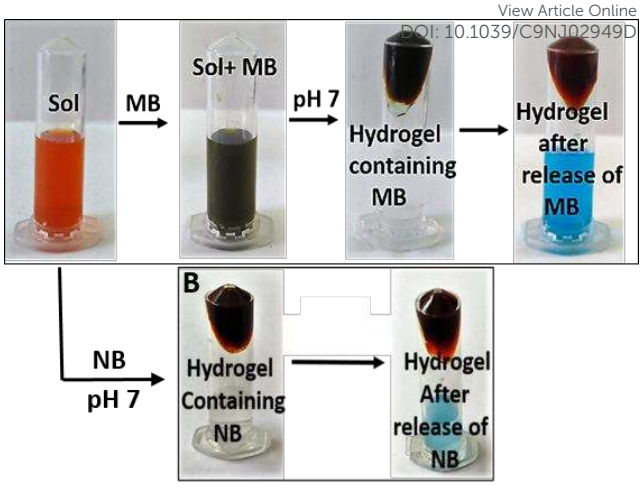

Fig. 14. Digital images depicting incorporation of MB (A) and NB (B) molecules into colloidal SPC3 followed by their gelation at pH 7 and release.

The adsorption of MB and its release profile on FD hydrogels is presented in Fig. S15. A comparison of Fig. 13 with Fig. S15 evidently shows that the loading as well as release of MB on the soft gel are more effective. For example, the loading of the soft gel has been found to be about more than two orders of magnitude higher, but its release was significantly slower to that of FD hydrogel.

3.16 Effect of external stimuli

The non-covalent nature of molecular hydrogels has been further probed by performing the effect of external stimuli like pH-, temperature- and sonication (Scheme 1). The hydrogels started to get converted into sol: below pH 5.5 in the acidic and beyond pH 8.5 in the basic medium; heating beyond 55 ^{0}C and sonication for 5 min, respectively. However, the complete transformation of hydrogels into transparent sol takes place at: pH 3 (in acidic medium) and pH 10.5 (in basic medium); temperature > 60 ^{0}C and sonication ≥15 min.

View Article Online
DOI: 10.1039/C9NJ02948D

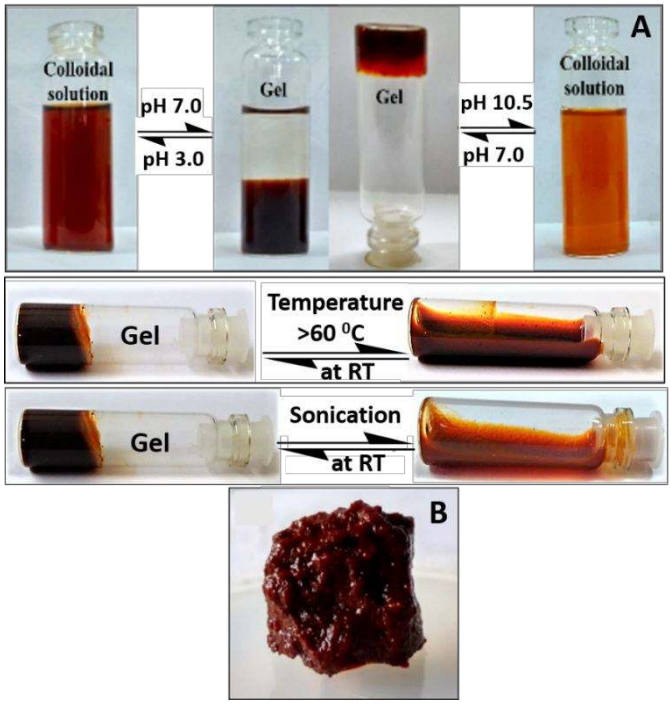

Scheme 1 (A) Digital images of colloidal solution of SPC3 depicting reversible transition into hydrogels (SPC3H) and back with a change in pH, temperature and sonication; (B) Digital photograph of solid hydrogel isolated at pH 7.

3.17 Cell viability study

The cytotoxicity of as synthesized hydrogel sample was examined by carrying out the cell viability for 293T human embryonic kidney cells, a representative of a cancer stem cell by running a control experiment under identical conditions in the absence of sample. The cytotoxicity was measured by performing the MTT assay which produced the purple color. It was monitored colorimetrically at 570 nm. These data exhibited the nontoxic behaviour of SPC3H within in the concentration range (μg/ml) of >125 - < 250 (Fig. S16).

Discussion

The formation of mechanically weak hydrogel at pH 5.8 in a slow process (about 4 days' time) (Fig. S17), and the production of relatively stronger gel rapidly (within 5 min) at pH 7 without any energy intensive treatment suggest it to be a curious observation. Moreover, as synthesized hydrogels demonstrating fully reversible sol-gel transition with a change in pH, temperature, and sonication evidently shows its chemical (pH) and physical stimuli (temperature and mechanical force) responsive behaviour (Scheme 1). These findings can be understood by the changed interaction(s) between β-FeOOH and 5'-CMP under different pH conditions.

The 5'-CMP has three electron donating N centre and is known to have four pKa(s): 4.5, 4.11, 6.3 and 0.8 corresponding to NH^+, NH_3^+, O=P-OH and P-OH, respectively.[41] Therefore, at different pHs the intensity of binding interactions between iron oxide phase and the functional groups of 5'-CMP (such as: $-NH_2$, C=O and $-PO_3^{2-}$) are expected to differ.

At pH 10.5 the OH- being stronger nucleophile may compete with the functional groups of 5'-CMP and will thus reduce its supramolecular interactions with β-FeOOH, hence transforming gel into the colloidal solution. Similarly, changes in interactions between 5'-CMP and β-FeOOH take place by increasing the temperature and prolonged sonication, leading to the conversion of gel into sol. All the above observations, *i.e.* the effect of pH, temperature and sonication (Scheme 1) clearly demonstrate the supramolecular nature of bonding among nanohybrids in the hydrogels, evidently suggesting it to be a soft material.

The UV-Vis (Fig. 2), Raman (Fig. 6) and IR (Fig. 7) spectroscopic data indicate that iron oxide in both the samples (SPC3 and SPC3H) to be present as β-FeOOH. The presence of iron in Fe^{3+} state in both SPC3H and SPC3 is clearly shown by XPS analysis (Fig. 8a and 8a'), which exhibited two doublets (eV) due to Fe $2p_{3/2}$ and Fe $2p_{1/2}$ along with a satellite peak at 718.0 eV matching to the previously described XPS data on β-FeOOH NPs.[35] It is further evidenced by XRD and SAED analyses, which, not only confirmed the formation of β-FeOOH phase but also indicated the growth of these nanostructures mainly along (112) and (103) planes unlike to that of the respective bulk phase, which is reported to have the most intense reflection along (101) plane. These changes can be assigned to the changed interaction(s) of 5'-CMP ligand with the core β-FeOOH during gelation.

The gelation observed by a change in pH as well as temperature requires to be analysed thoroughly in terms of the changed interactions among the core and shell under these conditions.

Based on the above findings, increased intermolecular interactions of 5'-CMP moieties present in the shell as well as with the core β-FeOOH within a building block at pH 4.3 (Scheme 2A) and among different building blocks at pH 7 (Scheme 2B) have been shown in Scheme 2. A number of such monomeric and dimeric metal complexes with 5'-CMP have earlier been investigated for their formation of several such metal crystals by recording their X- ray crystal structure.[75] The structures shown in Scheme 2 thus illustrate an increased non-covalent interaction of β-FeOOH with 5'-CMP molecule in SPC3H nanohybrids and relatively weaker interactions in SPC3, as has also been arrived by IR spectroscopy (Fig. S10; Table S3).

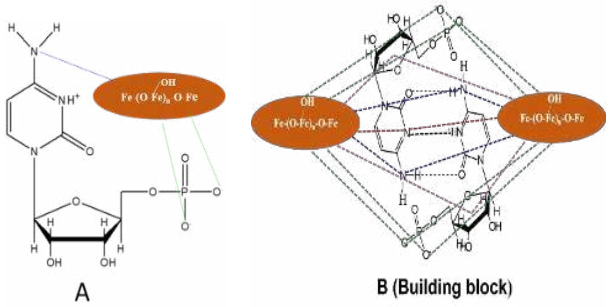

Scheme 2. Illustration of the non-covalent interactions in building block(s) of (A). SPC3 (pH 4.3); (B). SPC3H (pH 7.0) containing β-FeOOH and 5'-CMP building block(s).

View Article Online
DOI: 10.1039/C9NJ02949D

In literature similar supramolecular interactions involving chelation of metal centre through N3 and inter-ligand H- bond formation involving N4 amino group in 5'-CMP for a number of metal complexes have also been reported earlier on the basis of CD spectroscopy and X-ray crystal structure.[74,75] In a control experiment the participation of N containing functional groups was further probed by interacting cytidine with β-FeOOH under identical experimental conditions, which does not contain PO_3^{2-}. It also produced hydrogels, clearly indicating that the above observed interactions through N containing functionalities in 5'-CMP to be important for gelation.

A further deep analysis of interactions in SPC3H, observed in Raman and IR spectra, shows the appearance of a new peak at 852 cm^{-1} (in IR) and a shift in peak at 842 cm^{-1} to 839 cm^{-1} (in Raman). These bands are likely to be originated due to the angle deformation around N1'-C1'-O and C2'-C1'-O similar to those as have earlier been reported for cytidine.[64]

The angular deformation in the present case may be due to the puckering of ribose sugar (Scheme 3A), which might be resulting in increased interactions of β-FeOOH through different functional groups of 5'-CMP. This is also supported by the shift in Raman bands due to O3'C3'H, $-PO_3^{2-}$, C2'C1'H and rNH_2 groups to higher energy from 941, 986, 1138 cm^{-1} to 948, 994 and 1149 cm^{-1}, respectively. Apart from these, since the functional groups in IR (P-O str.), δ(C4'C5'H), δ(O3'C3'H) and rNH_2 are diminished; whereas the peak due to ribose sugar (νC4'O-νC4'C3'-δC3'O3'H)) observed in 5' -CMP is diminished. Besides, some new peaks are developed at lower (852 cm^{-1}) as well as at higher (1113 cm^{-1}) energies along with a minor shift in the frequency due to δ(C2'O2'H) from 1222 to 1216 cm^{-1} (Table S3). All these changes clearly suggest the puckering of ribose sugar in SPC3H, which results in increased interaction of Fe^{3+} through different functional groups of 5'-CMP to produce the hydrogels.

Among the two possible configurations of ribose sugar namely, C2'-endo or C3'-endo, since the peak due to sugar (ν (C4'O-νC4'C3'-δC3'O3'H)) is diminished along with the appearance of a new peak at 1113 cm^{-1} and the functionality, C2'O2'H is least affected in IR spectrum (Fig. 10), it evidently indicates the puckering of sugar ring upon gelation produces C3'-endo configuration. A reduction in the ellipticity of both positive and negative bands upon complexation with β-FeOOH in the gel also suggests the switching of conformation from C2'-endo to C3'-endo (Scheme 3A and 3B). In transition metal complexes of cytidine/nucleotides the puckering of ribose sugar has previously been shown to contain energetically favourable C3'-endo configuration because of their thermodynamic stability.[77]

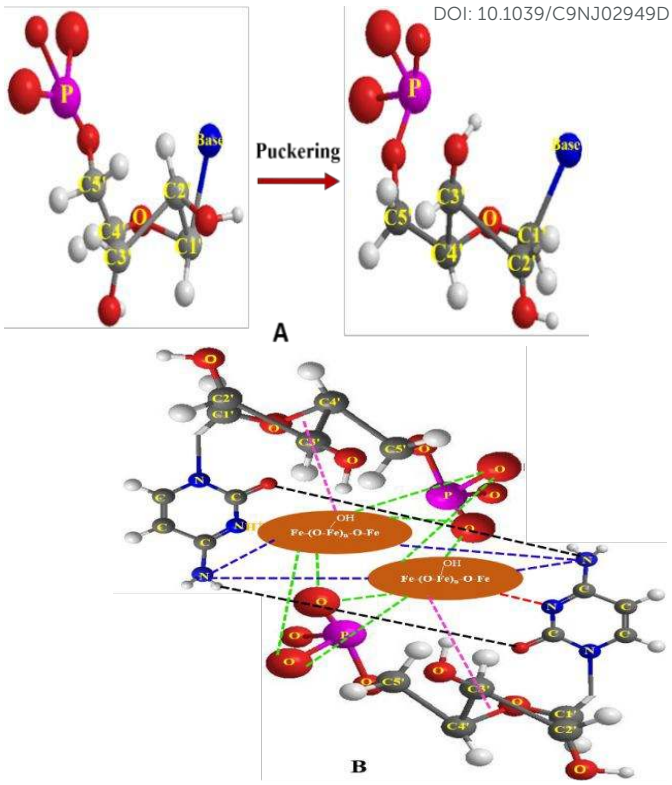

Scheme 3 (A) Puckering of ribose sugar in 5'-CMP; (B) Puckering of ribose sugar in the building block(s) 5'-CMP-β-FeOOH in SPC3H.

Based on the above spectroscopic data, the gelation observed in the process of self-assembly at pH 7 has been understood by increased intermolecular interactions among different building blocks (β-FeOOH and 5'-CMP) as was also evidenced by enhanced viscoelastic features such as higher storage modulus, LVR range, shear stress and yield strain in oscillatory measurements (Table S5). These interactions are shown in Scheme 4.

A change in the morphology from chains of nanoparticles (SPC3) into the porous structure in SPC3H is understood by the folding of chains in the self-assembly involving different building block(s) (5'-CMP- β-FeOOH). In fact, the core colloidal β-FeOOH nanoparticles being thermodynamically unstable attract each other over a long distance. However, the attractive and repulsive forces acting at the interface of electrical double layer of these colloidal particles, *i.e.* hydrophobic β-FeOOH core and the respective hydrophilic shell (5'-CMP) cause their reorientation/ reorganization so as to produce porous morphology (Scheme 4). In this respect the aggregated nanohybrids match to a micellar system.

View Article Online
DOI: 10.1039/C9NJ02949D

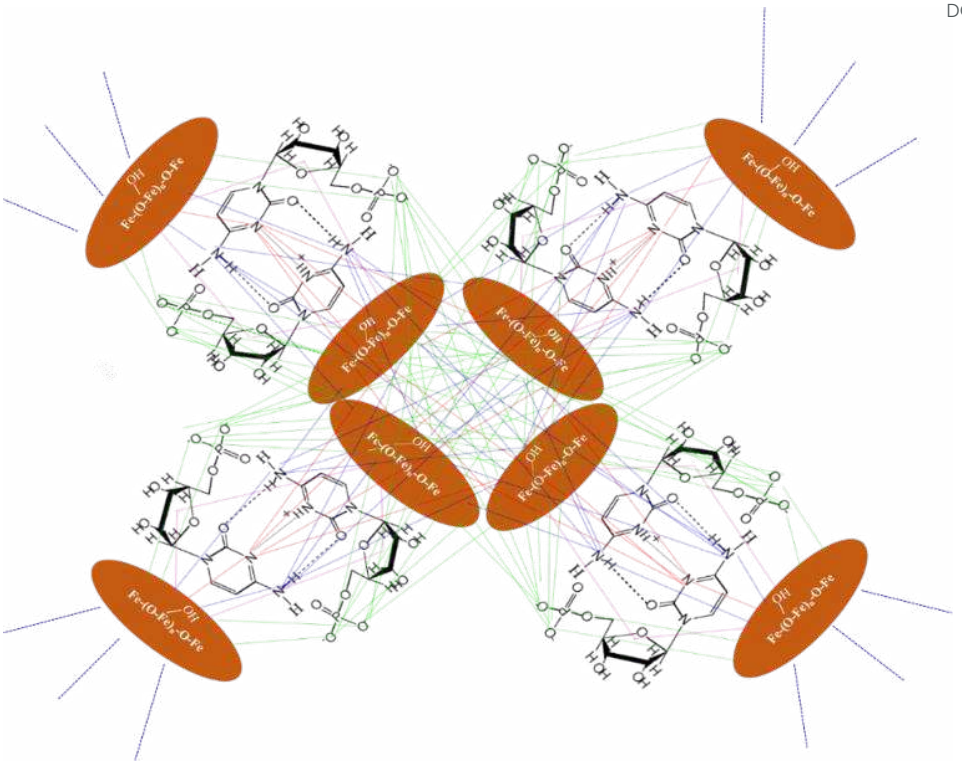

Scheme 4. Illustrating the increased supramolecular interaction among different building blocks of 5'-CMP-β-FeOOH nanohybrids leading to gelation.

The supramolecular interaction in the gel could be easily broken by heating as well as applying mechanical force. Interestingly, the gel could be restored back without any external stimuli, *i.e.* simply either upon centrifugation or by keeping the dispersed sol for a few minutes. Even the hydrogel sample with a partial cut undergoes self-repair evidently demonstrating the involvement of effective non-covalent interactions (Fig. 11 A).

To further verify the best gelation features of SPC3H at pH 7, the rheological measurements were also made at pH 5.8 (Fig. S17 and Table S7), which exhibited relatively poorer viscoelastic properties clearly supporting an increased solid like networking at pH 7.

To the best of our knowledge, previous reports on pyrimidine based nucleotide (5'-CMP) failed to produce hydrogels like structure[24,29,36] unlike to those of purine based nucleotides.[35-38] The non-formation of hydrogels in the bare 5'-CMP was also verified in the present work by designing a control experiment in which we have attempted to produce hydrogels under varied experimental conditions of: [5'-CMP] (2.5 to 60 mM) and pHs of (4; 7; and 9) and temperature (5 to 80 ^{0}C). In none of these conditions the gel formation could be observed, clearly suggesting the participation of β-FeOOH in the hydrogels formation. In order to substantiate this finding, a comparison of interaction(s) of 5'-CMP with different inorganics (nanoparticles/ metal ions/ and metal complexes) available in the literature has been presented in Table 1A.

An examination of Table 1A shows that the hydrogel formation takes place only in the presence of β-FeOOH nanoparticles. Notably, 5'-CMP interaction with Zn^{2+} and lanthanide ions does not produce hydrogels neither at pH 7.4 nor at 5.0, but under identical conditions the hydrogel formation takes place with purine based nucleotide, AMP.[24,29,36] In other reports 5'-CMP has been reported to simply undergo complexation with the metal(s) and added ligands.[70,75,76] Thus, we have clearly demonstrated the synthesis of the hydrogels employing biocompatible 5'-CMP under physiological conditions of pH 7 at room temperature; exhibiting rapid gelation, reversible sol-gel transformation under external stimuli with superior mechanical behaviour besides demonstrating self-healing and injectability features.

Further, a comparison of some physicochemical features of the present hydrogels with similar molecular and other types of hydrogels has been included in Table 1B.

View Article Online
DOI: 10.1039/C9NJ02949D

Table 1A. A comparison of interaction of 5'-CMP with different inorganic (nanoparticles, metal ions and metal complexes).

Nucleotides	Inorganic(s) /metal ions	Gelation/ Gelation time	Complex	pH	Sol –Gel transit-ion at pH	Mechanical properties	Ref.
5'-CMP	β- FeOOH	Hydrogel formed /< 5 min	-	7	3 and 10.5	Viscosity (cP)= 5557, G' = 4.02 × 10^4 Pa , G'' = 2.3 × 10^3 Pa, yield strain 8.1%, LVR 4%	Present work
5'-CMP	Zn^{2+} ions	No hydrogel formation	-	7.4	-	-	24,36
5'-CMP	lanthanide ions	No hydrogel formation	-	~5	-	-	29
5'-CMP	Co, Zn, Cd, Cu, Mn	-	Complexes:{[Co_2(CMP)$_2$(4,4'-bipy)$_2$ (H_2O)$_6$]·11H_2O}$_n$; [Co(5'-CMP)(H_2O)], [Zn(5'-CMP)(H_2O)], [Cd(5'-CMP)(H_2O)] . H_2O, [Cd_2(5'-CMP)$_2$(H_2O)$_2$].3H_2O,[Mn(5'CMP)(H_2O)].1.5 H_2O, [Cu(5'CMP)(2,2'-dipyridylamine) (H_2O)].5H_2O; {[Mn(bpe)(H_2O)$_4$]·(CMP)·3H_2O}$_n$, {[Co(bpe)(H_2O)$_4$]·(CMP)·3H_2O}$_n$	-	-	-	70,75,76

Table 1B. A comparison of physiochemical features of as synthesized soft molecular hydrogel over the other similar soft hydrogels.

Hydrogels (Soft molecular / polymeric)	pH/ magnetic behavior	Gelati-on Time /Mecha-nism	Response to External Stimuli	Inject-ability	Cyto-toxici-y	Self-healing	Drug loading (mg/g)	% Release at pH 7.0	Ref.
Zn, AMP* (5mM) (Soft molecular)	7.4	NR**/ NR	pH	NR	NR	Self-healed	NR	NR	24,36
La^{3+}, AMP* (Soft molecular) (1:2 molar ratio)	5.0	360 min / NR	pH	NR	NR	NR	NR	BSA release 75 %	29
La^{3+}, GMP* (50mM) (Soft molecular)	1.9 - 5.8	NR / NR	NR	NR	NR	NR	NR	NR	37
Ag, IMP* (10 mM) (Soft molecular)	NR	30 min / NR	pH	NR	NR	Self-healed	NR	NR	78
β-FeOOH, GMP* (2.5mM) (Soft molecular)	7.5/ Superpa-ramagne-tic	21 days / NR	NR	NR	Non-toxic	NR	NR	MB Soft gel NR FD gel ≥ 90	79; 35
β-FeOOH, CMP (2.5mM) (Soft molecular)	7.0/ Superpa-ramagne-tic	5 min/ Mecha-nism worked out	pH; Mechanic-al force; Temp.	Inject-able	Non-toxic	Self-healed	Soft gel =217 (MB); 7 (NB); FD gel = 0.9 (MB)	Soft gel ~ 99 (MB); > 75 (NB) FD gel > 91 (MB)	Pre-sent work
Chitosan based hydrogel	4	1h// NR	NR	NR	NR	NR	0.022 (mg/mL) (calculated)	NR	33
PVA-Fe_3O_4 (Polymeric)	NR/ Superpa-ramagne-tic	NR// NR	NR	NR	NR	NR	3.21 (Congo red)	≥50 (Congo red)	17

Bisaromatic hydrogelator (derived from isophthalic acid and urea) (synthetic)	1 (acidic)	NR// NR	pH	NR	NR	NR	800 (MB)	NR	80

View Article Online DOI: 10.1039/C9NJ02949D

* AMP denotes adenosine monophosphate; GMP denotes guanosine monophosphate; UMP denotes uridine monophosphate; IMP denotes inosine monophosphate; FD denotes freeze dried; MB denotes methylene blue; NB denotes nile blue

** NR stands for Not reported

An examination of Table 1B reveals that the loading and release of both the dyes in the present system are quite effective. Further, a comparison of the present system to those of previously reported hydrogels employing similar molecules reveals it to exhibit several additional features as regards to the reduced gelation time, response to more external stimuli, injectability, cytotoxicity, efficient drug loading and release (Table 1B). The loading of the drug onto hydrogels is understood to occur due to electrostatic interaction between them, which allowed to regulate the drug release into the aqueous medium of different pHs. Moreover, the advantage of the present soft supramolecular hydrogels over other types of hydrogels being used can be noted in its reversibility and inherent biological features such as biocompatibility, non-toxicity and targeting capabilities. All these findings display a significant green advance and sustainability over previously available hydrogel systems.

Thus the presently engineered hydrogels, consisting of biocompatible nucleotide and environmentally benign β-FeOOH NPs in superparamagnetic phase with interesting morphology and viscoelastic characteristics, displaying an efficient capability of adsorption and release of biologically important dyes (MB and NB) at room temperature suggest the as synthesized porous hydrogels to be the greener soft material with the potential for environmental and biomedical applications.

Conclusions

In summary, we have for the first time successfully synthesized, hitherto unreported, pyrimidine based nucleotide (5'-CMP) - mediated soft molecular hydrogel in aqueous medium. Interfacing of 5'-CMP molecule with nontoxic β-FeOOH NPs[48,49] produces porous hydrogels consisting of 5'-CMP-β-FeOOH nanohybrids. The supramolecular interactions between 5'-CMP with β-FeOOH NPs causes the puckering in 5'-CMP molecules resulting in a change in its conformation from C2'-endo to C3'-endo, which further enhances the non-covalent interactions among the nanohybrids in the self-assembly, assisting in the production of hydrogels. It is also manifested by the increased cross-linked solid network as revealed by fairly high values of viscosity, storage modulus, and shear stress. The rapid gelation of the colloidal solution 5'-CMP- β-FeOOH at pH 7 and its reversible transition into colloidal solution in both acidic as well as basic pH makes it a pH-responsive smart material. The reversible sol- gel transition is also revealed by the manipulation of temperature as well as by strain and stress. Thus, the chemical, thermal and mechanical stimuli could control the sol-gel transition.

The use of greener precursors (β-FeOOH and 5'-CMP) for the formation of as synthesized superparamagnetic hydrogels at physiological pH and temperature (37 °C), exhibiting low cytotoxicity, self-healing and injectable features suggest it to be biocompatible. Further, a fairly high values of storage modulus and other viscoelastic features, and its fast loading/adsorption and slow release capabilities for model drug/dye demonstrate it to be environmentally benign soft functional nanosystem. A variation in the behavior of release of the drug by a change in pH of the medium and with the amount of the loaded drug suggest its potential for drug delivery (Fig. 13).

This system thus presents a novel strategy for the fabrication of 5'-CMP mediated stimuli-responsive soft molecular hydrogels and overcomes the general drawbacks of polymeric hydrogels. This study clearly demonstrates it to be not only flexible and adaptable but also providing biocompatible safe matrix for the effective loading and release capabilities of drug/dye molecules. These distinctive characteristics evidently suggest its possible applications for drug delivery, wound healing, MRI contrast agent and environmental.

Conflicts of interest

There are no conflicts to declare.

Acknowledgements

The financial support of CSIR, New Delhi (Grant no. 01/ 2758/13/EMR-II) to undertake this work is gratefully acknowledged. Priyanka is thankful of MHRD, New Delhi for awarded SRF. We thank the Heads of IIC and MMED for providing me the facilities of XRD, AFM, TEM and SQUID. Thanks are also due to Dr. Vinit Kumar, Asst. Prof., Amity Institute of Molecular Medicine & Stem Cell Research, Amity Univ., Noida for performing the cytotoxicity experiments.

Notes and references

1 M. V. Ghica, M. Hîrjău, D. Lupuleasa and C. E. Dinu-Pîrvu, *Molecules*, , 2016, **21**, 786. DOI:10.3390/molecules21060786.

2 X. Hu, W. Wei, X. Qi, H. Yu, L. Feng, J. Li, S. Wang, J. Zhang and W. Dong, *J. Mater. Chem. B*, 2015, **3**, 2685–2697.

3 N. M. Barkoula, B. Alcock, N. O. Cabrera and T. Peijs, *Polym.*

Compos., 2008, **16**, 101–113.
4 B. Adhikari, G. Palui and A. Banerjee, *Soft Matter*, 2009, **5**, 3452–3460.
5 N. Sezgin and N. Balkaya, *Desalin. Water Treat.*, 2016, **57**, 2466–2480.
6 H. Guo, T. Jiao, Q. Zhang, W. Guo, Q. Peng and X. Yan, *Nanoscale Res. Lett.*, 2015, **10**, 0–9.
7 E. Caló and V. V. Khutoryanskiy, *Eur. Polym. J.*, 2015, **65**, 252–267.
8 E. Catalano and A. Di Benedetto, *J. Phys. Conf. Ser.*, 2017, 841. doi:10.1088/1742-6596/841/1/012010.
9 J. Li and D. J. Mooney, *Nat. Rev. Mater.*, 2016, 1, 12. doi:10.1038/natrevmats.2016.71.
10 C. Gao, J. Ren, W. Kong, R. Sun and Q. Chen, *RSC Adv.*, 2015, **5**, 90671–90681.
11 L. Zhang, S. R. Jean, S. Ahmed, P. M. Aldridge, X. Li, F. Fan, E. H. Sargent, S. O. Kelley, *Nat. Commun.* 2017*,* **8**, 381; DOI 10.1038/s41467-017-00298-w**.**
12 S. Lü, C. Gao, X. Xu, X. Bai, H. Duan, N. Gao, C. Feng, Y. Xiong and M. Liu, *ACS Appl. Mater. Interfaces*, 2015, **7**, 13029–13037.
13 W. Zhao, X. Jin, Y. Cong, Y. Liu and J. Fu, *J. Chem. Technol. Biotechnol.*, 2013, **88**, 327–339.
14 H. Wang and Z. Yang, *Nanoscale*, 2012, **4**, 5259–5267.
15 A. Jejurikar, X. T. Seow, G. Lawrie, D. Martin, A. Jayakrishnan and L. Grøndahl, *J. Mater. Chem.*, 2012, **22**, 9751–9758.
16 K. Shah, D. Vasileva, A. Karadaghy and S. P. Zustiak, *J. Mater. Chem. B*, 2015, **3**, 7950–7962.
17 L. Zhou, B. He and F. Zhang, *ACS Appl. Mater. Interfaces*, 2012, **4**, 192–199.
18 S. B. Campbell, M. Patenaude, T. Hoare, S. B. Campbell, M. Patenaude and T. Hoare, Biomacromolecules, 2013, **14,** 644-653.
19 E. M. Ahmed, *J. Adv. Res.*, 2015, **6**, 105–121.
20 R. Tian, J. Chen and R. Niu, *Nanoscale*, 2014, **6**, 3474–3482.
21 L. A. Estroff and A. D. Hamilton, *Chem. Rev.*, 2004, **104**, 1201–1217.
22 J. Dash, A. J. Patil, R. N. Das, F. L. Dowdall and S. Mann, *Soft Matter*, 2011, **7**, 8120–8126.
23 X. Du, J. Li, Y. Gao, Y. Kuang and B. Xu, *Chem. Commun.*, 2012, **48**, 2098–2100.
24 F. Pu, J. Ren and X. Qu, *Chem. Soc. Rev.*, 2018, **47**, 1285–1306.
25 G. M. Peters and J. T. Davis, *Chem. Soc. Rev.,* 2016, **45**, 3188-3206.
26 A. Kumar and V. Kumar, *Chem. Rev.*, 2014, *114*, 14, 7044–7078.
27 H. Liang, S. Jiang, Q. Yuan, G. Li, F. Wang, Z. Zhang and J. Liu, *Nanoscale*, 2016, **8**, 6071–6078.
28 D. Das, T. Kar and P. K. Das, *Soft Matter*, 2012, **8**, 2348–2365.
29 L. Xu, Z. Zhang, X. Fang, Y. Liu, B. Liu and J. Liu, *ACS Appl. Mater. Interfaces*, 2018, **10**, 14321–14330.
30 X. Du, J. Zhou, J. Shi and B. Xu, *Chem. Rev.*, 2015, **115**, 13165–13307.
31 B. Escuder and J. F. Miravet, https://pubs.rsc.org, 2013, doi:10.1039/9781849737371-FP001.
32 R. Dong, Yan Pang, Yue Su and X. Zhu, *Biomater. Sci.,* 2015, **3**, 937-954.
33 G. Tronci, H. Ajiro, S. J. Russell, D. J. Wood, and M.Akashi, *Acta Biomaterialia,* 2014**, 10**, 821–830.
34 J. Li, E. Weber, S. Guth-Gundel, M. Schuleit, A. Kuttler, C. Halleux, N. Accart, A. Doelemeyer, A. Basler, B. Tigani, K. Wuersch, M. Fornaro, M. Kneissel, A. Stafford, B. R. Freedman, and D. J. Mooney, *Adv. Healthcare Mater*. 2018**,** **7**, 1701393.
35 A. Kumar and S. K. Gupta, *J. Mater. Chem. B*, 2013, **1**, 5818–5830.
36 H. Liang, Z. Zhang, Q. Yuan and J. Liu, *Chem. Commun.*, 2015, **51**, 15196–15199.
37 J. Zhang, X. Li, X. Sun, A. Song, Y. Tan and J. Hao, *Sci. China Chem*. 2018, **61**, 604–612.
38 Y. Hu, D. Xie, Y. Wu, N. Lin, A. Song and J. Hao, *Chem. Eur. J.* 2017, **23,** 15721–15728.
39 Assessment of nutrient requirements for infant formulas, *J Nutr*. 1998, 128, 2059S-2293S.
40 A. Gella, J. Ponce, R. Cussó and N. Durany, *J. Physiol. Biochem.*, 2008, **64**, 9–17.
41 E. Rodríguez-Gonzalo, J. Domínguez-Álvarez, M. Mateos-Vivas, D. García-Gómez and R. Carabias-Martínez, *Electrophoresis*, 2014, **35**, 1677–1684.
42 L. M. Janas and M. F. Picciano, *Pediatr. Res*, 1982, **16**, 659–662.
43 J. K. Oh and J. M. Park, *Prog. Polym. Sci.*, 2011, **36**, 168–189.
44 D. Shi, M. E. Sadat, A. W. Dunn and D. B. Mast, *Nanoscale*, 2015, **7**, 8209–8232.
45 L. Machala, R. Zboril and A. Gedanken, *J. Phys. Chem. B*, 2007, **111**, 4003–4018.
46 R. Gonzalez-rodriguez, P. Granitzer, K. Rumpf and J. L. Coffer*, R. Soc. Open Sci.* 2018, **5**, 180697.
47 M. Magro, S. Domeneghetti, D. Baratella, P. Jakubec, G. Salviulo, E. Bonaiuto, P. Venier, O. Malina, J. Tuček, V. Ranc, G. Zoppellaro, R. Zbořil and F. Vianello, *Chem. -A Eur. J.*, 2016, **22**, 14219–14226.
48 M. L. Chen, L. M. Shen, S. Chen, H. Wang, X. W. Chen and J. H. Wang, *J. Mater. Chem. B*, 2013, **1**, 2582–2589.
49 L. Zeng, W. Ren, J. Zheng, A. Wu and P. Cui, *Appl. Surf. Sci.*, 2012, **258**, 2570–2575
50 Z. Wang, Y. Ma, H. He, C. Pei and P. He, *Appl. Surf. Sci.*, 2015, **332**, 456–462.
51 J. Zhao, W. Lin, Q. Chang, W. Li and Y. Lai, *Environ. Technol. Rev.*, 2012, **1**, 114–126.
52 E. A. Deliyanni, E. N. Peleka and K. A. Matis, *Sep. Sci. Technol.*, 2007, **42**, 993–1012.
53 X. Guo and F. Chen, *Environ. Sci. Technol.* 2005, **39,** 6808-6818.
54 J. Cai, J. Liu, Z. Gao, A. Navrotsky and S. L. Suib, *Chem. Mater*. 2001, **13**, 4595–4602.
55 Z. Xu, J. Liang and L. Zhou, *Open J. Inorg. Non-Metallic Mater.*, 2013, **3**, 58–65.
56 R. Purbia and S. Paria, *ACS Appl. Nano Mater.* 2018**, 1**, 1236−1246.
57 Y. Yusim, D. Livingstone and A. Sidi, *J. Clin. Anesth.*, 2007, **19**, 315–321.
58 M. Blue, *Clin. Trials*, 2017, **6099**, 2017.
59 C.W. Lin, J. R. Shulok, S. D. Kirley, L. Cincotta, and J. W. Foley, C*ancer Res.* 1991, **51**, 2710-2719.
60 J. Madsen, I. Canton, N. J. Warren, E. Themistou, A. Blanazs, B. Ustbas, X. Tian, R. Pearson, G. Battaglia, A. L. Lewis, and S. P. Armes*, J. Am. Chem. Soc*. 2013, **135**, 14863−14870.
61 S. Petrova , Y. Kostov , K. Jeffris and G. Rao, *Analytical*

View Article Online
DOI: 10.1039/C9NJ02949D

Lett., 2007, **40**, 715–727.
62 C. Luna, M. Ilyn, V. Vega, V. M. Prida, J. González and R. Mendoza-Reséndez, *J. Phys. Chem. C*, 2014, **118**, 21128–21139.
63 S. Das and M. J. Hendry, *Chem. Geol.*, 2011, **290**, 101–108.
64 M. Mathlouthi and J. L. Koenig, *Carbohydrate Res.* **1986**,146, 1-13.
65 M. De La Fuente, A. Hernanz and R. Navarro, *J. Biol. Inorg. Chem.*, 2004, **9**, 973–986.
66 K. Okamoto, V. Benham and T. Theophanides, *Inorganica Chim. Acta*, 1987, **135**, 207–210.
67 S. A. Lee, M. Schwenker, A. Anderson and L. Lettress, *J. Raman Spectrosc.*, 2004, **35**, 324–331.
68 E. Murad and J. L. Bishop, *Am. Mineral.*, 2000, **85**, 716–721.
69 C. A. Sprecher and W. C. Johnson, *Biopolymers*, 1977, **16**, 2243–2264.
70 P. Zhou, J. F. Yao, C. F. Sheng and H. Li, *CrystEngComm*, 2013, **15**, 8430–8436.
71 Q. M. Qiu, P. Zhou, L. Gu, L. Hao, M. Liu and H. Li, *Chem. - A Eur. J.*, 2017, **23**, 7201–7206.
72 Y. Işikver, *Fibers and Polymers* 2017, **18**, 2070-2078.
73 P. K. Sukul and S. Malik, *RSC Adv***.,** 2013**, 3**, 1902–1915.
74 H. Maeda and Y. Maeda, *Langmuir*, 2011, **27**, 2895–2903.
75 K. Aoki and W. Saenger, *J. Inorg. Biochem.*, 1984, **20**, 225–245.
76 P. Zhou, C. Wang, Q. M. Qiu, J. F. Yao, C. F. Sheng and H. Li, *Dalt. Trans.*, 2015, **44**, 17810–17818.
77 P. Collery, *Metal Ions in Biology and Medicine: Proceedings of the Fourth International Symposium on Metal Ions in Biology and Medicine Held in Barcelona (Catalonia), Spain, on May 19-22, 1996*,(John Libbey Eurotext, 1996).
78 N. Thakur, B. Sharma, S. Bishnoi, S. K. Mishra, D. Nayak, A. Kumar and T. K. Sarma, *ACS Sustainable Chem. Eng*. 2018, **6**, 8659−8671.
79 A. Kumar and S. K. Gupta, *J. Phys. Chem. B* 2014, **118**, 10543−10551.
80 F. Rodrı´guez-Llansola, B. Escuder, J. F. Miravet, D. Hermida-Merino, I. W. Hamley, C. J. Cardin and W. Hayes, *Chem. Commun.*, 2010, **46**, 7960–7962.

Graphical abstract

View Article Online
DOI: 10.1039/C9NJ02949D

Environmentally benign pH-responsive cytidine-5'-monophosphate molecule-mediated akaganeite (5'-CMP-β-FeOOH) soft supramolecular hydrogels induced by the puckering of ribose sugar with efficient loading/release capabilitie

Anil Kumar* and Priyanka

Department of Chemistry,
Indian Institute of Technology Roorkee,
Roorkee- 247667, Uttarakhand, INDIA.
E-mail: anilkfcy@iitr.ac.in; akmshfcy@gmail.com; Tel.. +91-1332-285799; Fax. +91-1332-273560

Novel synthetic protocol for environmentally benign 5'-CMP-β–FeOOH soft hydrogels exhibiting rapid pH-responsive reversible sol-gel transition, efficient adsorption slow release capabilities is reported.